Materials Today Communications 31 (2022) 103266

Contents lists available at ScienceDirect

Materials Today Communications

journal homepage: www.elsevier.com/locate/mtcomm

Electron beam evaporated vs. magnetron sputtered nanocolumnar porous stainless steel: Corrosion resistance, wetting behavior and anti-bacterial activity

Stefania Bobaru [a], Víctor Rico-Gavira [b,*], Aurelio García-Valenzuela [b], Carmen López-Santos [b,c], Agustín R. González-Elipe [b]

[a] BSH Electrodomésticos España, S.A. (CIV-TME), Avda. de la Industria 49, 50016 Zaragoza, Spain
[b] Nanotechnology on Surfaces and Plasma laboratory, Instituto de Ciencia de Materiales de Sevilla (CSIC-Univ. Sevilla), Avda. Américo Vespucio 49, 41092 Seville, Spain
[c] Departamento de Física Aplicada I, Universidad de Sevilla, Calle Virgen de Africa 7, Seville E-41011, Spain

ARTICLE INFO

Keywords:
Stainless steel coatings
Nanocolumnar thin films
Wetting
Corrosion
Anti-bacterial activity
Oblique angle deposition
MS
Abrasion

ABSTRACT

Stainless steel (SS), widely used because of its outstanding corrosion protection properties, does not possess any particular anti-stain or anti-bacterial activity as required for household and sanitary applications. This work reports the fabrication of SS thin films that, keeping a similar corrosion resistance than the bulk material, presents hydrophobicity and anti-bacterial activity. These thin films are prepared at ambient temperature by physical vapor deposition (PVD), either electron beam evaporation (EBE) or magnetron sputtering (MS), at oblique angles (OAD). According to their scanning electron microcopy and atomic force microscopy analysis, the microstructure of the OAD-SS thin films consisted of tilted and separated nanocolumns defining a surface topology that, characterized by a high percentage of void space, varied with the deposition conditions and procedure, either EBE or MS. It has been shown that particularly the nanocolumnar MS-OAD thin films preserved and even improved the high corrosion resistance of compact SS, as determined by electrochemical analysis. Besides, all OAD-SS thin films depict hydrophobicity and a high antibacterial activity. These features, particularly remarkable for the MS-OAD thin films, have been related with their tip-like termination at the surface and the existence of large void spaces separating the nanocolumns. This topology appears to affect negatively the bacteria's deployment onto the surface and therefore the survival rate. Differences in the corrosion and anti-bacterial performance between EBE and MS-OAD thin films have been related with the specificities of these two PVD methods of thin film preparation. A relatively high abrasion resistance, as determined by abrasion tests, supports the use of MS-OAD thin films for the protection of commodity materials.

1. Introduction

Stainless steel (SS) is the generic designation of a large variety of metallic alloys containing iron as main component. Chromium and other transition elements in addition to carbon are also incorporated in the alloy in order to bestow it a high resistance against corrosion. Due to their outstanding properties, the use of these alloys is pervasive for a large variety of applications and their large scale production is the basis of one of the most important industrial activities worldwide [1]. Generally, SS alloys are utilized in compact form and as such are prepared as bulk laminates or monolithic samples. Some essays have also been made with SS alloys in the form of compact thin films, which prepared by magnetron sputtering (MS), [2–6] thermal spray coating, [7] atomic layer deposition, [8] ultrafast laser pulse interaction with stainless steel surfaces, [9,10] or by selective laser melting (SLM), [11] aim at achieving the corrosion resistance and other properties typical of bulk steel alloys. However, SS alloys have not been prepared in the form of nanostructured and porous thin films where its intrinsic properties might be modulated by specific growing forms or nanostructures. A very efficient and, at the same time, relatively simple way of preparing nano-columnar thin films is by Physical Vapor Deposition at oblique angles (OAD) [12]. By this method the vaporized material flux arrives

* Corresponding author.
E-mail address: victor@icmse.csic.es (V. Rico-Gavira).

https://doi.org/10.1016/j.mtcomm.2022.103266
Received 4 May 2021; Received in revised form 7 January 2022; Accepted 8 February 2022
Available online 11 February 2022

onto a planar substrate forming a high angle with respect to the surface perpendicular (i.e., typical zenithal angles of arrival higher than 70º) and therefore at a glancing angle with respect to the surface. Under these conditions the deposited material adopts the form of a very porous and tip-terminated layer formed by tilted nanocolumns with a high volume percentage of void space among them [13,14].

The present work investigates the possibilities of this kind of SS alloy thin films to confer surface hydrophobicity and antibacterial properties while preserving the typical anticorrosion behavior of this material in compact form. In fact, previous investigations with titanium and other metals grown by MS-OAD techniques have revealed an enhanced antibacterial response of their surfaces, a behavior that has been related with a negative effect of the nanocolumn tips on the growth, deployment and stabilization of biofilms [15,16]. Although the origin of this deleterious effect on bacterial growth is still controversial, it has been empirically associated with surfaces formed by nanocolumn heads of some tenths of nm separated by surface voids in this range of sizes [17,18]. Therefore, in this work we firstly analyze the morphological and chemical characteristics of a series of nanostructured SS alloy thin films prepared by e-beam evaporation (EBE) and magnetron sputtering (MS) in an OAD configuration (i.e., OAD SS alloy thin films). Then, relevant properties of the synthesized nanocolumnar SS alloy layers are systematically studied as a function of their specific nanostructure and surface roughness. In concrete, we investigate the anticorrosion, [2] wetting [6,11] and antibacterial properties [9] of these nanostructured SS alloy thin films. The hydrophobicity and outstanding antibacterial performance depicted by the OAD SS alloy layers has been related with their singular surface nanostructure. The significantly improved performance of MS vs. EBE films has been discussed in relation with the differences expected for the growing mechanisms of the two type of OAD thin films [19]. The relatively high stability of the nanostructured OAD layers when subjected to abrasion resistance tests, [20] particularly those prepared by MS, has proved their suitability for real applications in domains such as food packages or household appliances.

2. Experimental

2.1. Synthesis and characterization of nanostructured SS alloy thin films

SS alloy thin films were prepared by OAD changing the zenithal deposition angle between the surface normal and the impinging direction of particles onto de substrates assuming that they follow straight trajectories. Schemes of the operating modes by EBE or MS are reported in the Supporting information Fig. S1.

The pellets of the SS alloy (AISI 301) used for e-beam evaporation were purchased from the commercial manufacturer Equipment Support Company U.S.A., Inc. and used without further manipulation. EBE thin films were prepared at room temperature at zenithal angles of 0º (i.e., normal configuration) and 70º, and 85º (i.e., EBE-OAD thin films), as described in previous works [21]. These films are named indicating their thickness in nm and the evaporation angle, e.g., EBE400–85 refers to a SS alloy based thin film of 400 nm thickness prepared by evaporation at 85º. For comparative purposes, EBE thin films of pure metallic iron were also deposited in the same experimental set-up.

Nanocolumnar SS alloy based thin films were also prepared by magnetron sputtering in an OAD configuration (MS-OAD) at a zenithal angle of incidence of 85°. A 3″ SS-target (AISI 301 with purity 99.999%, Kurt J. Lesker) was assembled to a magnetron head and excited with an average power of 200 W in pulsed-DC mode at a frequency of 80 kHz and 2.5 μs off-time. The sample holder was placed at a distance of 7 cm from the target center. The base pressure in the reactor chamber before the experiments was below 5×10^{-6} mbar. An argon gas (purity 99.995%) pressure of 2×10^{-3} mbar was kept constant during the depositions using a flow rate of 12.5 sccm. Although thin films with different thickness were prepared by this procedure, results will only be reported for sample MS750–85. This choice was justified because this sample presented a nanocolumnar morphology similar to that of the much thicker films EBE1500–85 and, as reported in the results section, the maximum surface roughness of the whole series.

Thin films were deposited on quartz plates, silicon wafers and 0.4 mm thick SS foils (AISI 301) with a bright-annealed (BA) finished termination provided by ACERINOX (Spain). For simplicity, from now on we will used the general designation “SS thin films” to refer to the EBE and MS thin films prepared from pellets or targets of the corresponding SS alloys. However, it is noteworthy that composition and crystallinity of the thin films may differ from these properties of typical SS materials. In particular, since the characterization analysis of the EBE thin films showed a preferential deposition of some of the constituent elements in the pellets with respect to other (see results section), EBE thin film deposition was carried out using new pellets for each new fabrication essay. No significant variation in composition as a function of thickness was found for the MS thin films and therefore the analysis of film performance focused on sample MS750-85.

Surface morphology of the SS thin films was determined by scanning electron microscopy (SEM) for thin films deposited on silicon wafers, which were diced for cross section imaging. This analysis was carried out in a Hitachi S4800 field emission microscope. Average size of surface motifs was analyzed on the SEM images with the ImageJ software.

Surface topography of the SS OAD thin films grown on silicon was examined by atomic force microscopy (AFM) in a Dulcinea microscope from Nanotec (Madrid, Spain), which was working in tapping mode using high-frequency cantilevers. Roughness, expressed in the form of RMS values, was determined from the AFM images using the WSxM free available software provided by Nanotec [22]. Bearing area plots were determined by the height distribution histogram over each AFM analyzed surface. These plots indicate the measured surface area above and below a certain height. Center of the bearing area plot was obtained through the derivative function of the bearing area distribution with respect to the height.

Atomic ratios between constituent elements of the films were determined by X-ray fluorescence (XRF) in a Panalytical (model AXIOS) spectrometer provided with a Rh tube for the elemental analysis of samples. The determined atomic compositions agreed with those measured by EDX in the SEM microscope.

Surface composition and chemical state of the atoms at the surface of the deposited films were determined by X-ray photoemission spectroscopy (XPS) in a PHOIBOS HSA3500 spectrometer, working with pass energy of 15 eV. Binding energy (BE) calibration of the energy scale of the spectra was done assigning a BE of 284.6 eV to the C 1 s peak due to airborne contamination. Error bars for XRF and XPS analysis refer to the typical variations expected for these determinations according to the manufacturer.

Crystalline structure of the films was analyzed by X-ray diffraction using the Cu Kα radiation with a Panalytical X′Pert Pro diffractometer incorporating a diffracted beam graphite monochromator and 1D silicon strip detector (X′Celerator).

2.2. Functional properties of OAD SS thin films

A standardized 1720 abrasion and wash-ability tester manufactured by Elcometer and provided by an abrasive element integrating a sponge and an abrasive textile pad was employed to perform series of linear abrasion tests under dry conditions with a load of 0.05 Kgf/cm^2.

Wetting behavior of thin films deposited on BA-SS foils was determined by the sessile droplet method measuring the static and hysteresis contact angles, SCA and HCA, this latter calculated as the difference between advancing and receding dynamic contact angles [23,24]) of water droplets of 1 and 3 μL, respectively. For the determination of surface energy values, [25,26] drops of double-distilled water with a volume of 1 μL and diiodomethane with a volume of 3 μL were dispensed on the samples surfaces and their contact angles measured by the sessile drop method. Surface tension values taken for water were $\sigma_a = 72.8$ mJ

m^{-2}, $\sigma_a^P = 51$ mJ m^{-2}, $\sigma_a^D = 21.8$ mJ m^{-2} and for diiodomethane, $\sigma_b = 50.8$ mJ m^{-2}, $\sigma_b^P = 44.1$ mJ m^{-2}, $\sigma_b^D = 6.7$ mJ m^{-2}, where σ^D, the dispersive component and σ^P, the polar component of the surface tension, were taken from the bibliography [27,28]. The analysis of wetting properties was carried out for aged samples stored in a dissector at least for one month after their preparation. Letting stabilize the surface state of fresh-prepared metallic samples was important in order to stabilize the wetting properties, since their surface state evolved from superhydrophilic in the "as prepared" state to a steady state hydrophobic situation after prolonged storage in air [29].

Corrosion properties of the SS nanocolumnar films deposited onto flat foils of this material were assessed by electrochemical analysis using the potentiodynamic polarization method (i.e., by means of the polarization plots to determine significant corrosion parameters [30]). The electrochemical tests were carried out in a standard three-electrode cell using the deposited thin films as working electrode, a counter-electrode made of a stainless steel rod and a reference electrode consisting of a saturated calomel electrode (SCE). The potential of the SCE was + 241 mV versus NHE at 25ºC. A potentiostat Autolab was used for the electrochemical measurements. All electrochemical measurements were carried out at ambient temperature using an aerated 0.5 wt% NaCl solution as electrolyte. Determination of relevant electrochemical parameters (e.g., corrosion and pitting potentials, corrosion and passive current) from the polarization plots has been carried out as indicated in ref [30]. The following specific parameters were used for the potentiodynamic polarization tests carried out in this work: scan rate of 2 mV s^{-1} and a potential range from − 1 (−1.25) to + 1.5 V that was scanned in the anodic direction. The corrosion current density I_c was determined by extrapolation of Tafel slopes taken at the potentiodynamic polarization curves at + −250 mV below and above the corrosion potential. Approximate values of passive current density I_p were taken at the medium position of the passivation zone observed in the potentiodynamic polarization diagrams. Corrosion and pitting potentials, E_c and E_p, were determined following the accepted convention by the analysis of the potentiodynamic polarization diagrams [30].

Two bacterial growth tests were carried out using the gram-negative *Escherichia coli (E.Coli)* bacteria, one of the most common bacteria found in industrial and domestic SS surfaces. Tests were carried out for thin films deposited onto flat BA-SS foils. *Test 1* is a common fluorescence method used to determine biofilm formation by fluorescence microscopy [31]. The following protocol was applied: in the middle of each SS sample, 100 μL of bacterial stock (~107 cfu/ml) was seeded and a biofilm was generated by placing these samples in an incubator for 48 h at 37 °C. After this incubation period, samples were rinsed with distilled and sterilized water to remove non-adherent bacteria. Then, 20 μL of dye solution from the LIVE/DEAD®BacLight™ Bacterial Viability Kit (L13152) were added to the samples. This kit contains two dyes, the SYTO 9 dye which enters into viable and dead cells and emits green fluorescence, and the Propidium Iodide (PI) (red fluorescence) dye that only enters into dead cells, masking the green fluorescence emitted by the SYTO 9 dye. As a result, viable and dead cells are visualized with a green and red fluorescence, respectively. A cover slip was placed over the dye and the sample was kept for 15 min in the dark. Biofilm was visualized with an Epifluorescence Microscope, OLYMPUS BX53.

Test 2 aimed at the quantification of the number of living bacteria onto the samples after a certain period of time. For this purpose, 50 μL of an E.Coli bacterial stock of known concentration was dripped in the middle of the 2cmx2cm sample and a cover slip placed above it. Three tests were done for each sample utilizing bacterial suspensions with three levels of dilution (10^3, 10^4 and 10^5). The samples were placed in sterile Petri dishes and then inserted in a moisture chamber that was placed into the incubator for 24 h at 37 °C. To determine the bacteria concentration, bacteria cells cultured onto the samples were removed and sown onto agar plates. Then the agar plates were introduced into an incubator and kept there for 24 h at 37 °C to count number of colonies forming units (cfu). Then, this number was corrected by the dilution factors utilized to drip the bacteria solution onto the samples in order to estimate the total number of lived bacteria remaining onto the different samples. This value was the average of the three tests carried out for each sample. The logarithm of the number of viable bacteria cells onto the reference sample (i.e., a flat SS surface of compact thin films) and onto the test samples (the tip headed SS surfaces of nanostructured films) was taken as a quantification parameter (i.e., results will be expressed as the logarithm of the reduction of microbial growth onto the nanostructured samples with respect to the reference SS foil). The error bar considered for these values take into account the expected deviations of the actual number of bacteria within each cfu.

3. Results

3.1. Structure, microstructure and chemistry of SS thin films

All SS films were amorphous when examined by XRD, a feature that contrast with the crystalline character of iron thin films prepared by OAD (see Supporting information Fig. S2).

Fig. 1 shows a series of normal and cross-section views SEM micrographs taken for EBE400–70, EBE400–85 and EBE1500–85 thin films deposited onto a silicon substrate. A similar nanostructure at local scales was found for equivalent thin films deposited onto the flat BA-SS substrates used for functional property tests, as it can be seen in the Supporting information, Fig. S3. According to micrographs in Fig. 1 and S3, SS films evaporated in a normal geometry (EBE400–0) presented a relatively compact microstructure with low roughness and a compact surface morphology made of grains with a size smaller than 20 nm. This contrasts with the highly porous and columnar nanostructure of the EBE-OAD films prepared at 70º and 85º. According to the micrographs in Fig. 1, both nanocolumn widths at the surface and separation distance between tilted nanocolumns increase with the thickness and deposition angle of the films. It is also apparent in this figure that increasing the deposition angle renders a rougher surface termination with larger nanocolums width and hollows, always in the order of tenths nms. Tilting angle of nanocolumns in EBE thin films was slightly higher (i.e., 45º and 50º for samples EBE400-70 and EBE400–85) than for pure metallic iron (40º and 44º at these two angles, see Supporting information Fig. S4), but still within the values expected for metal thin films according to current models accounting for the growth mechanism of OAD thin films [19]. On the other hand, the SEM analysis of sample MS750–85 shows that its microstructure also consists of nanocolumns, somehow similar to those of sample EBE1500-85 (see Fig. 1c), but with an inclination angle of approximately 40º. It is noteworthy that, despite the apparent similarities in microstructure, thickness of sample MS750–85 is half that of sample EBE1500–85, a feature stressing the differences in OAD thin film fabrication by EBE or MS, already discussed in previous works [32]. Along this paper we will comment about the differences between the EBE and MS thin film growth mechanism, which being particularly noticeable for OAD conditions, [19] can explain the improved behavior of MS-OAD thin films for anti-corrosion and anti-bacterial applications.

A careful AFM analysis of the surface topography of EBE thin films (see AFM maps in Supporting information, Fig. S5) revealed a clear evolution with thickness and deposition angles. The average RMS values of the films determined from these images clearly proved that roughness progressively increases for the thicker films prepared at higher angles (see the values in Table 1, where roughness values are presented together with relevant wetting parameters of samples that will be discussed later). This characterization also revealed that sample MS750–85 presented the maximum roughness of all examined samples. Therefore, we may conclude that thickness, deposition angle (for EBE thin films) and preparation technique (MS vs. EBE) affect the roughness of the films.

Regarding the antibacterial behavior of the examined SS thin films, besides roughness it is also relevant to consider the surface

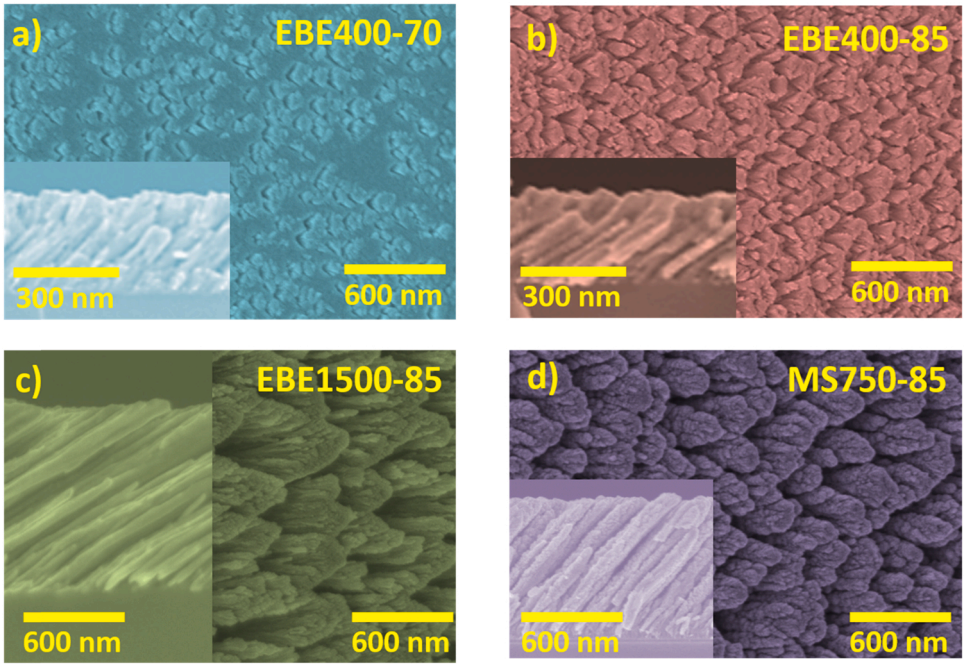

Fig. 1. - Normal and cross section (insets) micrographs of OAD SS thin films onto silicon: (a) EBE400-70 (b) EBE400-85 c) EBE1500-85, d) MS750-85.

Table 1.
Static contact angles, hysteresis angles, roughness and surface energy of SS thin film samples.

SAMPLE	RMS[1] (nm)	SCA (°)[2]	HCA (°)[3]	γ_{tot} [mN/m][4]
EBE400–0	3.0	84	22	36.2
EBE150–70	3.1	103	21	32.1
EBE400–70	3.9	97	33	39.5
EBE1500–70	5.4	113	42	14.5
EBE150–85	8.9	112	30	28.6
EBE400–85	9.2	85	38	40.2
EBE1500–85	14.2	97	49	26.7
MS750–85	17.5	120	25	51.7

1.-Surface Roughness determined from AFM images (c.f., Fig. S5); 2.-Static contact angles; 3.-Hysteresis contact angles; 4.- Surface energy.

inhomogeneity that, expressed as differences in surface heights, can be statistically evidenced by the so-called Bearing area plots [33]. Bearing plots diagrams determined for the studied samples are shown in Fig. 2. The center of the height distributions can be identified by the maximum of the derivative of the Bearing area plots. Derivative curves reveal that surface topography of EBE thin films prepared at 70° of zenithal angle

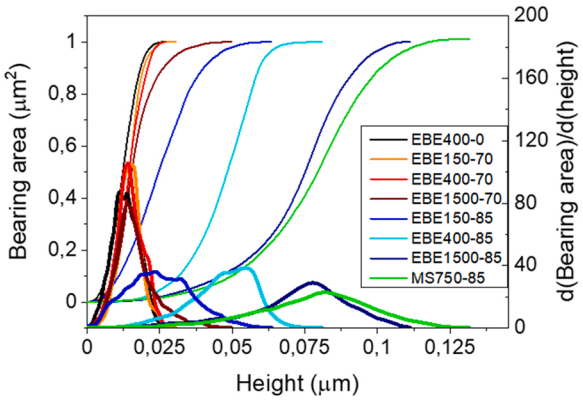

Fig. 2. - Bearing area plots of the examined samples deduced from AFM images and derivatives of the Bearing area plots (right y-axis).

presents surface inhomogeneities in height that on average peak at around 10–15 nm, independently on thickness. However, surface heterogeneity of EBE thin films prepared at a zenithal deposition angle of 85° highly increase with thickness, varying from a derivative maximum at 25 nm for sample EBE150-85 to ca. 78 nm for sample EBE1500–85. Meanwhile the spam of the Bearing area plots also increase with thickness and this tendency supports that surface heterogeneity increases with this parameter. In the light of these considerations it is also remarkable that sample MS750-85 presents the highest surface heterogeneity from the whole series with a derivative maximum peaking at ca. 82 nm. By this analysis of the surface topography it is also relevant the fact that the average size of surface features increases with thickness, as determined by analysis of the SEM images with the software ImageJ (see Supporting information Fig. S6). For example, 52030 nm^2 and 61070 nm^2 values were determined for samples EBE400-85 and EBE1500-85 and a maximum value of 122817 nm^2 for sample MS750–85. We will discuss below how an increasingly higher surface heterogeneity contributes to the antibacterial properties of these thin films.

In comparison with the target material, the EBE films presented significant variations in the Fe/M (M: Cr + Ni) ratios as a function of the film thickness. Fig. 3 shows, in the form of a bar diagram, the evolution with thickness of the Fe/M ratio determined by XRF for the films prepared in the OAD configuration (i.e. at 70° and 85° for EBE films and at 85° for the MS films) and at normal geometry (i.e., at 0°). It is apparent in this figure that, with respect to the XRF data for the target/pellet material, the films were depleted in iron and that, for the EBE thin films, the content of this element changed with thickness, independently on deposition angle. The progressive enrichment in iron for the thicker SS thin films, even if remaining lower than the Fe content in the target material, indicates that a preferential evaporation of Ni and Cr takes place during thin film deposition and that there is a progressive compensation of this effect as the target becomes impoverished in these two elements during the growth process. These results prove that the composition of EBE films is heterogeneous in thickness and only approaches the composition of the target material for relatively thick films. Unlike this evolution of atomic composition for the EBE films, the MS films presented a rather constant composition in thickness that approaches the composition of the thickest EBE films. An enrichment in

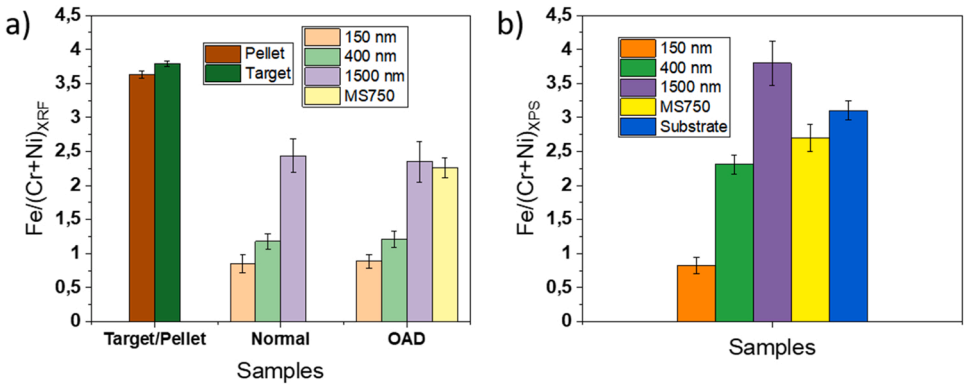

Fig. 3. - a) Bar diagram representing the Fe/(Cr+Ni) ratio determined by XRF as a function of thickness for the EBE-SS films prepared in normal (i.e., 0º evaporation angle) and OAD (i.e., 70º and 85º of evaporation angle) configurations and for the MS OAD film prepared at 85º. The Fe/(Cr+Ni) ratio determined in the pellets and target used for evaporation is included for comparison. b) Value of the Fe/(Cr+Ni) ratio determined by XPS for the EBE thin films as a function of thickness and for the MS thin film. The ratio obtained at the surface of the stainless-steel substrate is included for comparison.

Cr/Ni with respect to that in bulk SS may contribute to modify the film properties, as explained in next sections.

Surface composition in the form of Fe/(Cr+Ni) values (c.f., Fig. 3) was also determined by XPS (probing depth around 20 Å) for the EBE films, showing a progressive surface enrichment in iron with the film thickness. Meanwhile, the MS thin film presented a Fe/(Cr+Ni) ratio rather similar to that in the bulk. However, in neither case Ni could not be detected by this technique at the surface of the films, indicating a relative surface enrichment of Cr. In addition, the analysis of the shape and binding energies of the Fe2p and Cr2p peaks revealed that these elements are oxidized at the surface in the form of Fe_2O_3 [34,35] and Cr_2O_3 [36] (see Supporting information Fig. S7). It is also noteworthy that the analysis by XPS showed a higher degree of surface contamination by carbonaceous rests for the EBE (ratio C/Fe= 10) than for the MS thin films (ratio C/Fe= 2.6) (see Supporting information Fig. S7).

3.2. *Abrasion resistance of SS OAD thin films*

Besides hydrophobicity, anticorrosion and antibacterial properties, abrasion stability is an additional requisite for thin films intended as surface terminations of household elements, plastics or similar appliances [1,37,38]. As example of the abrasion resistance of OAD thin films, Fig. 4 shows a series of normal SEM micrographs taken for samples EBE400-0, EBE400-70, EBE400-85 and MS750-85 subjected to a different number of abrasion cycles in a normalized abrasion test intended to characterize the surface resistance of household elements. Images show that after 300 abrasion cycles, film nanocolumns in sample EBE400-85 are still present on the surface, although their tip have acquired a rounded shape evidencing a certain removal of material from the outer surface of nanocolumns. However, SEM images suggested a higher removal after 1000 cycles. Meanwhile, EBE400-70 thin films

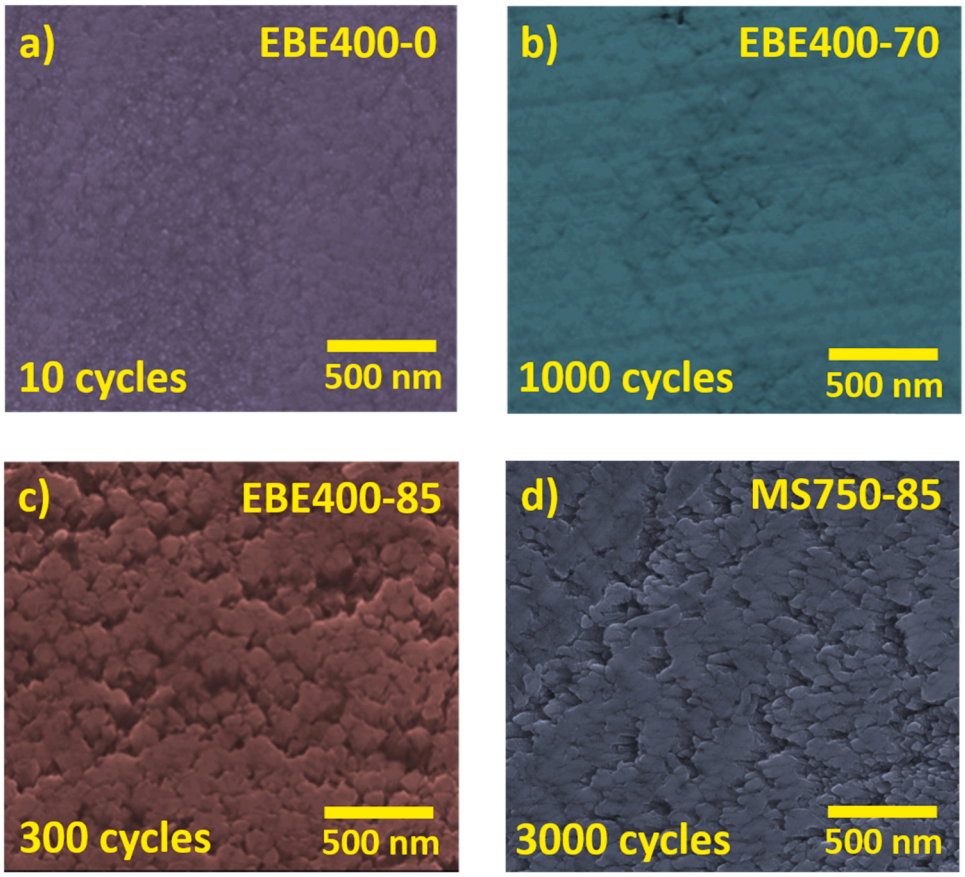

Fig. 4. - Normal SEM micrographs of samples EBE400-0 (a), EBE400-70 (b), EBE400-85 (c) and MS750-85 (d) subjected to the indicated abrasion tests..

with a higher surface density of nanocolumns and less roughness presented a higher abrasion resistance as exemplified by the micrograph in Fig. 4b) taken after 1012 abrasion cycles and where the nanocolumnar structure is still clearly devised. However, it is the most remarkable that the columnar features of sample MS750-85 remained almost intact after 3000 abrasion cycles, this sample depicting the maximum abrasion resistance from the whole series. This behavior justifies the use of these samples for applications where they are going to be subjected to moderate handling abrasion as expected for household elements.

3.3. Wetting behavior of SS OAD thin films

All SS films were hydrophilic (WCA around 30º or less) just after their preparation, but similarly to other fresh metal surfaces, thin films or laser ablated bulk metals, [29,39] their contact angle progressively increased with time to reach steady state values after storage for approximately one month. This process was accompanied by a progressive contamination of the SS thin film surfaces, as confirmed by the XPS determination of an increase in the C1s signal of airborne carbonaceous residues at the surface of the stored samples. This behavior is common to other fresh metal surfaces prepared by evaporation or laser ablation procedures [40] and, in our case, it occurred to a larger extent for the EBE-OAD than for the MS-OAD thin films as evidenced by the XPS analysis of these samples (c.f., Fig. S7) [29,41–43].

The roughness and wetting parameters of the aged samples collected in Table 1 support a neutral or a mild hydrophobicity both for the compact EBE400-0 and the other EBE OAD thin films after aging. This is confirmed by their SCAs with values around or above 90º and their HCA values around 30º, indicating a petal-like behavior characterized by a relatively high adhesion and a low roll-off capacity for water droplets (roll-off angles between 40º and 90º were determined depending on sample). The picture is complemented with the determination of relatively low surface energies for the thin film samples [27,28]. Overall, this analysis of the wetting behavior of the EBE thin films reveals that aged samples were moderately hydrophobic and that the actual wetting angle was rather dependent on the contamination degree, and therefore history, of the surface. In turn, sample MS750-85 was clearly hydrophobic (WCA of 120º), although presented a certain adhesion capacity towards water droplets as indicated by a HCA value similar to that of the flatter thin films. Remarkably, this sample presented the maximum roughness (RMS) that, according to common wetting models, (29, 33) can be a decisive factor for its hydrophobic behavior with a WCA higher than that of the other samples. Very likely, this surface roughness factors is sufficient to counterbalance the relatively higher surface energy also found for this sample. It is also noteworthy that although sample MS750–85 has the maximum corrosion resistance from the whole set of samples (see next section), we do not claim any direct correlation between wetting and corrosion properties and relate the latter with the differences in the inner microstructure of the nanocolumns stemming from the EBE and MS preparation procedures.

3.4. Corrosion of SS OAD thin films

Corrosion resistance of OAD SS films was tested using the potentiodynamical polarization method [2,7,9,30,44]. Fig. 5 a)-b) shows series of these plots for EBE-OAD thin films of increasing thickness prepared at 70º and 85º deposition angles and also for sample EBE400–0 and a SS foil included for comparison. A plot for sample MS750–85 is also reported in Fig. 5c) in comparison to the plots of a SS foil and sample EBE1500–85.

The visual analysis of these plots and the analysis of the derived corrosion parameters gathered in Table 2 suggest that SS thin films have a significant corrosion resistance that approaches that of the SS foil, with some differences depending on deposition angle, thickness and deposition procedure (EBE or MS) as discussed next. Data show a little but progressive evolution of the corrosion potential (E_c) from a value similar to that of the SS foil to slightly more negative values as the thickness of

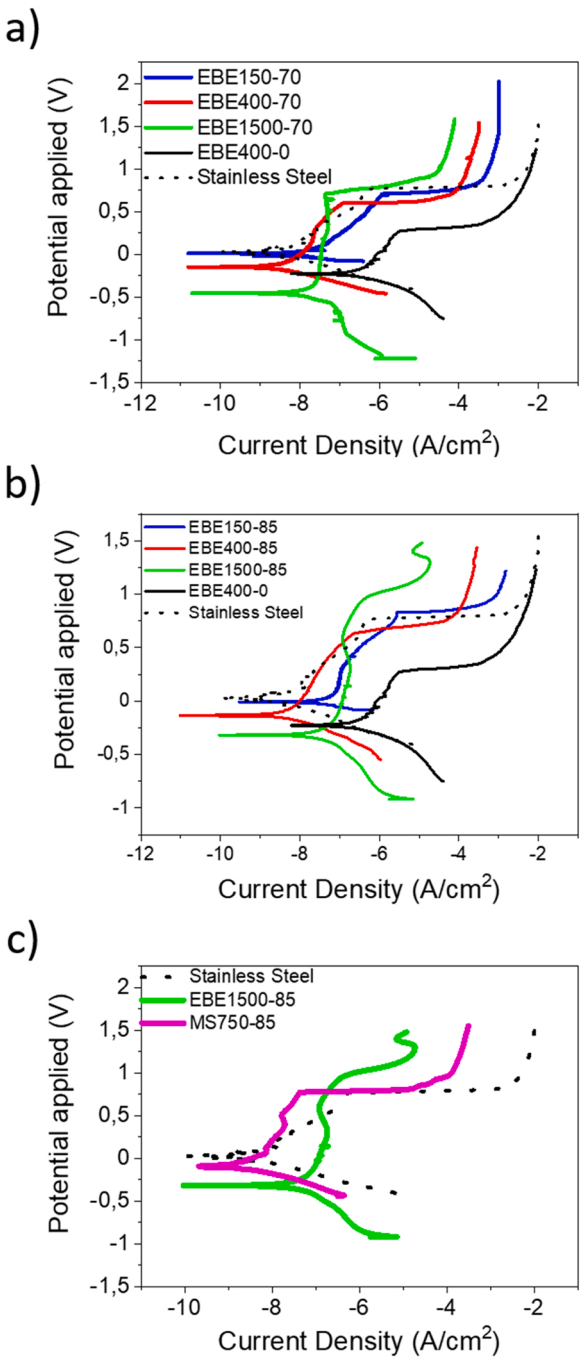

Fig. 5. - Potentiodynamic polarization curves recorded for the EBE OAD thin films prepared at 70º (a) and 85º(b). Equivalent plots for the SS foil and samples EBE400–0 thin films are included for comparison. c) Plot recorded from the MS750-85 thin film compared with the equivalent curves for the SS foil and sample EBE1500-85.

the EBE films increases (i.e. plots in Fig. 3a) and b)), while the deposition angle has little effect on this parameter. In addition, the potentiodynamic polarization curves of EBE samples, including sample EBE400–0, show relatively similar passive currents (I_p) for rather similar pitting potentials (E_p) in most cases (note however that not a proper passivation zone, typically characterized by a constant I_p for increasing potentials, develops in the examined SS samples, including the reference). It is also apparent that the voltage difference between the pitting and corrosion potentials (i.e., Ep-Ec), is similar or higher for the EBE thin films than for the SS foil and increased with thickness, particularly for the thickest

Table 2
Main corrosion parameters derived from the potentiodynamic polarization curves of samples.

Sample	E_C (V)	E_p (V)	E_p-E_C (V)	I_c[1] (A/cm^2)	I_p[2] (A/cm^2)
SS	0.02	0.76	0.74	5.3E-9	3.3E-7
EBE400-0[a]	-0.23	0.27	0.50	6.6E-7	1.0E-6
EBE150-70	0.01	0.71	0.70	1.4E-8	5.4E-6
EBE400-70	-0.18	0.66	0.84	1.1E-8	5.5E-7
EBE1500-70	-0.45	0.70	1.15	2.8E-8	2.3E-7
EBE150-85	0.01	0.75	0.76	3.9E-8	5.1E-6
EBE400-85	-0.13	0.63	0.76	6.3E-9	4.7E-7
EBE1500-85	-0.32	0.98	1.30	5.3E-8	6.3E-6
MS750-85	-0.09	0.78	0.86	6.6E-9	7.1E-7

1.- Determined by Tafel plot analysis.
2.- Approximate value determined at an intermediate position of the passivation region in the potentiodynamic polarization diagram.
[a] Experiments conducted for samples EBE150–0 and EBEB1500–0 render values that did not significantly vary with respect to that of sample EBE400–0.

films. This indicates that the EBE thin films present a specific corrosion resistance that, for the thinner films, can be related with the relative enrichment of Cr determined by XRF and XPS analysis. On the other hand, the corrosion current density (I_c), determined by Tafel slope analysis of the polarization curves, was always higher for the EBE films (either OAD or normal) than for the SS foil, a feature that we link with the much higher specific surface of the EBE-ODA thin films and/or their low compactation (e.g., for sample EBE400–0 where no nanocolumns are formed) due to the low kinetic energy of evaporated atoms forming their structure [32].

On the other hand, the importance of Cr in determining a high corrosion resistance of the OAD SS thin films can be illustrated comparing the corrosion resistance of the OAD SS thin films and equivalent films of pure iron. Thus, although measured Ec and calculated I_c for OAD thin films of pure iron (see plot for samples Fe400–0, Fe400–70 and Fe400–85 in the Supporting information, Fig. S8**;** note the difficulty to accurately determine Ic by Tafel slope analysis) present values of − 0.15 V and over 10E-7 A cm^{-2} that are similar to those of OAD SS thin films, the passivation zone observable in the potentiodynamic polarization curves is very small for iron, clearly indicating that not a passive layer is formed in this case as expected from the lack of chromium in its formulation (a rough estimation from the diagrams renders very little E_c-E_p values around 0.1–0.2 V, which indicate that no effective passive layer is formed in the analysis medium).

Within the previous scheme of analysis, it is quite relevant the behavior of sample MS750–85, characterized by I_c, I_p, E_c, E_p and E_p-E_c values rather similar to those found for the SS foil. The quite small I_p value found for this sample supports an effective protection by the passive layer formed during the positive polarization scan. This means that despite the highly porous and nanocolumnar character of this kind of thin films, they withstand corrosion as well as a compact SS foil does. The higher corrosion resistance of the MS-OAD with respect to that of the EBE-OAD thin films points to a different internal structure of the nanocolumns in each case. This difference is particularly relevant when comparing samples EBE1500–85 and MS750–85, the former depicting values of E_c, I_c and I_p clearly suggesting a less corrosion resistance in the saline medium, despite that it has a double thickness than the latter (note however, the higher values of E_p and E_p-Ec determined for sample EBE1500–85, indicating that the protection against pitting is more effective in this sample). Although this point is outside the scope of the present paper we can argue the known fact that the deposition process during EBE is purely ballistic with particles bearing only thermal energy (0.1–0.3 eV), while particles during MS deposition bear up to ten or more eVs of kinetic energy, a difference contributing to the atomic lattice mobilization of deposited atoms [32]. As a result EBE-OAD nanocolumns would present a high concentration of atom vacancies and small nanopores that are not present in the more compact nanocolumns developed during MS-OAD deposition, a difference probably linked with the slightly different corrosion resistance of these two kinds of thin films. Additional evidences of the smaller corrosion resistance of EBE thin films can be extracted by the SEM observation of sample SS400–85 after the potentiodynamic polarization analysis. The obtained images show the destruction of nanocolumns and their substitution by patches spotted onto the surface that must correspond to the segregation of iron oxide during the electrochemical oxidative scan (see Supporting information Fig. S9).

The higher corrosion resistance revealed by the polarization tests for the OAD thin films in comparison with that of the EBE400–0 layers prepared in a normal configuration agrees with some evidences in the literature for nanostructured coatings of other metals like Ti [44], various metal alloys [45], or SS thin films prepared by MS in a normal configuration [2], but confronts the results of other works with nanostructured and/or porous metal films, metal glasses or multilayers reporting a degradation in the corrosion resistance for nanostructured surfaces [46,47]. As already mentioned, a possibility to account for the evolution in the corrosion resistance parameters in Table 2 is that the higher Cr relative content found in the evaporated films contributes to their corrosion resistance. This would agree with other results in the literature where Cr enrichment in iron glasses [10] or depletion in cathodic arc evaporated SS [48] lead to improvement or degradation of corrosion resistance, respectively. However, the reason why this stabilization role mainly occurs in samples prepared in an OAD configuration, and is particularly noticeable for the MS-OAD thin films, are not completely clear at this point. We hypothesize that some restrictions to the out diffusion of oxidized cationic species through the void channels of the nanocolumn structure of OAD thin films might contribute to this behavior. In favor of this hypothesis is the fact that the thicker the thin films are the more corrosion resistance they are, despite that the content of Cr decreases with thickness.

3.5. *Antibacterial properties of SS thin films*

Avoiding bacterial deployment and biofilm formation are crucial characteristics of biomaterials and household components, usually subjected to specific surface treatments [49]. Herein, we have investigated the antibacterial activity of OAD SS thin films looking to their ability to prevent the bacterial growth on their surface. For these experiments, a particular care was taken to use samples aged for the same period of time after their preparation (i.e., one month) that were stored under the same conditions until performing the antibacterial tests. We must note though that differences in surface contamination/hydrophobicity character cannot be completely excluded.

Fig. 6left) shows colored fluorescent optical microscope images of the bacteria cultured on EBE400–85 and MS750–85 thin films compared with an equivalent image obtained for the SS substrate (i.e., *Test1*, see experimental section). The black images spotted with red dots in the 2mmx2mm fluorescence images taken for samples EBE400–85 and MS750–85 indicate that the surface of these thin films is only covered by dead bacterias. These results prove that surface nanostructuration reduces the capability of the bacteria to deploy in the form a biofilm either due to a reduction in bacteria adhesion and/or because colonies die after formation.[17] Unlike this antibacterial behavior of SS OAD thin films, the surface of SS foil substrates was not bactericide and the image in Fig. 6 left) shows the existence of numerous living bacterias on its surface, as evidenced by the green colored stains typical of extracellular bacterial colony matrixes [15].

To quantitatively assess the antibacterial activity, we also estimated the reduction of living bacteria on the surface of films applying the *Test 2* described in the experimental section. The plot in Fig. 6 right) shows a representation of the logarithm of reduction of bacteria growth on the selected SS OAD thin films with respect to that found on the SS reference. This parameter is represented in this figure as a function of the maxima determined from the Bearing area derivative curves in Fig. 2.

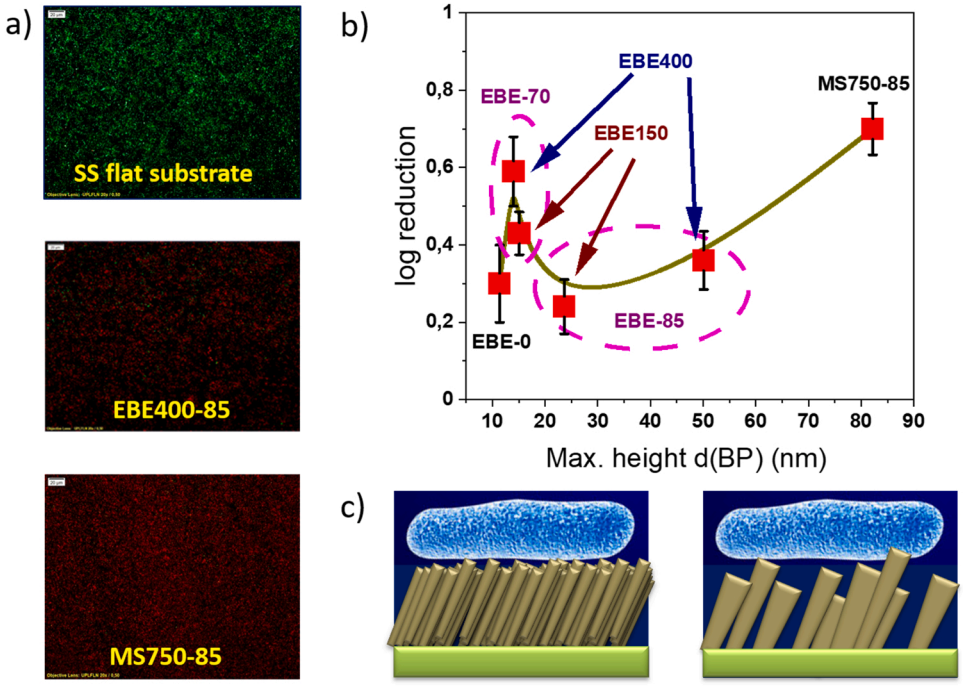

Fig. 6. - a) Fluorescent optical images of the surface of EBE400-85 and MS750-85 and SS substrates after bacterial deployment test (Test1, see experimental section). b) Representation of the Log of the reduction in the number of bacterial grown on the studied samples with respect to SS substrates (Test 2, see experimental section) represented as a function of their roughness expressed as the maxima of Bearing area derivative plots. Pink contours highlight EBE thin films prepared at 70° and 85° deposition angles. The green line is plotted to guide the eye. c) Scheme showing a representation of a bacteria sitting on nanocolumnar surfaces with a relatively low roughness and surface hetereogeneity as expected for thin films prepared at 70° deposition angle (left) and high roughness surface heterogeneity as expected for sample MS750-85. (For interpretation of the references to color in this figure legend, the reader is referred to the web version of this article.)

The plot confirms that EBE and MS OAD thin films present a clear anti-bacterial behavior with values of log reduction ranging from ca. 0.2–0.7. The data point are somehow scattered, making it difficult to draw direct conclusions about the factor(s) favoring this anti-bacterial activity. For example, sample EBE400-0, depicts a clear reduction in bacterial growth with respect to the SS foil. A possibility could be that the poor corrosion resistance of this sample, its amorphous character and the relative enrichment in Cr with respect to a SS foil might contribute to reduce the number of lived bacteria cells through the release of traces of this element when in contact with the bacteriaś seeded liquid used for this test. However, the similar or higher values of the log of reduction of bacterias growth found for the more corrosion resistant EBE-OAD samples must be accounted for by other contributions. In line with previous studies on bacteriaś growth on nanocolumnar thin films of other metals [9,15,17] or oxides [50] we attribute a key anti-bacterial effect to the tip terminated surface topology of these samples. In agreement with the results in these works and according to the scheme in Fig. 6c), bacterias feel inappropriate such a tip-ended surfaces and do not efficiently deploy onto them. This was proved in our study by the SEM observation that the few bacterias remaining on the OAD thin films after *test 2.* The few remaining bacterias rounded themselves on the surface, suggesting that they try to minimize the interface contact area with the tip-terminated surface (see Supporting information Fig. S10). Within this framework, the maximum reduction of bacteriaś growth found for sample MS750-85 (i.e., log reduction of ca. 0.7) supports that its irregular tip-surface topology is key for the observed antibacterial activity. In fact, this sample presented the highest corrosion resistance from the whole series of OAD samples and was even more effective against corrosion than the SS-foils (c.f. Fig. 5 and Table 2). This clearly discards some poisoning by leached chromium or another element as a differential factor explaining its antibacterial behavior. Meanwhile, the fact that sample MS750-85 presents the maximum surface heterogeneity from the whole set of studied samples (c.f. Fig. 2) confirms the assessment above that surface topology is a key factor of antibacterial activity of OAD thin films.

4. Conclusions

The previous results and discussion have revealed that SS thin films prepared by evaporation or magnetron sputtering at oblique angles present a nanocolumnar microstructure similar to that of metals prepared by the same procedure. The wetting behavior of the SS nanostructured films was relatively similar to that of other metal surfaces prepared by other methods in the sense that OAD SS films were superhydrophilic just after preparation and became neutral or moderately hydrophobic after aging for one month. This evolution has been linked with their surface contamination with airbone hydrocarbons.

These SS OAD thin films, despite their high porosity and nanocolumnar microstructure, present a good anticorrosion behavior, which was comparable and even slightly superior for the MS-750–85 films than that of flat SS substrates. In addition, contrary to SS foils, OAD thin films presented a very good antibacterial behavior and effectively hindered the growth and deployment of bacterias onto their surface. The enrichment of chromium in the nanocolumnar structure and its leaching during bacterias seeding tests and the tip terminated roughness of the OAD films are deemed synergetic factors contributing to this behavior. In this picture it is remarkable the superior performance of the MS-OAD thin films in terms of abrasion and corrosion resistance and enhanced antibacterial activity. The higher compactness of nancolumns formed in these thin films in comparison with the relatively high internal porosity of EBE nanocolumns and layers is proposed as the main factor accounting for these differences. The combination of good anticorrosion and therefore chemical stability, high anti-bacterial activity and a reasonably good abrasion resistance make MS-OAD thin films good candidates for applications such as household protection or health material coatings.

CRediT authorship contribution statement

Stefania Bobaru: Methodology, Investigation, Data curation, Visualization, Writing – review & editing. **Víctor Rico-Gavira:** Conceptualization, Methodology, Investigation, Data Curation, Visualization, Supervision, Writing – review & editing, Funding acquisition. **Aurelio García-Valenzuela:** Methodology, Investigation, Writing – review & editing. **Carmen López-Santos:** Methodology, Investigation, Data curation, Visualization, Writing – review & editing. **Agustín R. González-Elipe:** Conceptualization, Methodology, Investigation, Data curation, Visualization, Writing – original draft, Writing – review &

editing.

Declaration of Competing Interest

The authors declare that they have no known competing financial interests or personal relationships that could have appeared to influence the work reported in this paper.

Acknowledgments

Authors thank the FEDER program and AEI-MICINN (PID2019-110430GB-C21, PID2019-109603RA-I0 and PID2020-112620GB-I00), the Consejería de Economía, Conocimiento, Empresas y Universidad de la Junta de Andalucía (PAIDI-2020 through projects US-1263142, ref. AT17-6079, P18-RT-3480), and the EU through cohesion fund and FEDER 2014–2020 programs for financial support. The projects leading to this article have received funding from the EU H2020 Program under the grant agreements 899352 (FETOPEN-01-2018-2019-2020 - SOUNDofICE). One of us (SB) acknowledges the support of the Marie Curie Program of the EU to carry out this work. BSH is acknowledged for having proposed this work and contributed to its realization. CLS thanks the University of Seville through the VI PPIT-US.

Appendix A. Supporting information

Supplementary data associated with this article can be found in the online version at doi:10.1016/j.mtcomm.2022.103266.

References

[1] Asm Handbook: Properties and Selection: Irons, Steels, and High Performance Alloy, 10th Edition ed., 1993.
[2] C. Lopez-Melendez, R.G. Bautista-Margulis, E.M. Garcia-Ochoa, H.E. Esparza-Ponce, C. Carreno-Gallardo, C. Gaona-Tiburcio, J. Uruchurtu-Chavarin, A. Martinez-Villafane, Evaluation of corrosion resistance of thin films 304 stainless steel deposited by sputtering, Int. J. Electrochem. Sci. 7 (2012) 1149–1159.
[3] M.P. Ryan, N.J. Laycock, H.S. Isaacs, R.C. Newman, Corrosion pits in thin films of stainless steel, J. Electrochem. Soc. 146 (1999) 91–97.
[4] G.T. Burstein, S.P. Vines, Repetitive nucleation of corrosion pits on stainless steel and the effects of surface roughness, J. Electrochem. Soc. 148 (2001) B504–B516.
[5] C. Pan, L. Liu, Y. Li, B. Zhang, F.H. Wang, The electrochemical corrosion behavior of nanocrystalline 304 stainless steel prepared by magnetron sputtering, J. Electrochem. Soc. 159 (2012) C453–C460.
[6] P. Yiu, J.D. You, S.T. Wang, J.P. Chu, Tunable hydrophilicity in a surface nano-textured stainless steel thin film deposited by DC magnetron sputtering, Appl. Surf. Sci. 555 (2021).
[7] S.M. Gateman, K. Page, I. Halimi, A.R.C. Nascimento, S. Savoie, R. Schulz, C. Moreau, I.P. Parkin, J. Mauzeroll, Corrosion of one-step superhydrophobic stainless-steel thermal spray coatings, ↱ACS Appl. Mater. Interfaces 12 (2020) 1523–1532.
[8] A.K. Singh, K. Adstedt, B. Brown, P.M. Singh, S. Graham, Development of ALD coatings for harsh environment applications, ACS Appl. Mater. Interfaces 11 (2019) 7498–7509.
[9] A.A. Nastulyavichus, S.I. Kudryashov, I.N. Saraeva, N.A. Smirnov, A.A. Rudenko, E. R. Tolordava, D.A. Zayarny, S.A. Gonchukov, A.A. Ionin, Nanostructured steel for antibacterial applications, Laser Phys. Lett. 17 (2020) 6.
[10] Z. Wang, E.-M. Paschalidou, A. Seyeux, S. Zanna, V. Maurice, P. Marcus, Mechanisms of Cr and Mo enrichments in the passive oxide film on 316L austenitic stainless steel, Front. Mater. 6 (2019) 232.
[11] Z.W. Wang, L.D. Shen, M.B. Qiu, W. Jiang, Y. Chen, J.F. Zhao, Study on the properties of superhydrophobic coating prepared by scanning electrodeposition on SLM substrate, Mater. Res. Express 6 (2019) 10.
[12] A. Barranco, A. Borras, A.R. Gonzalez-Elipe, A. Palmero, Perspectives on oblique angle deposition of thin films: from fundamentals to devices, Prog. Mater. Sci. 76 (2016) 59–153.
[13] M.M. Hawkeye, M.J. Brett, Glancing angle deposition: fabrication, properties, and applications of micro- and nanostructured thin films, J. Vac. Sci. Technol. A 25 (2007) 1317–1335.
[14] W. Phae-ngam, C. Chananonnawathorn, T. Lertvanithphol, B. Samransuksamer, M. Horprathum, T. Chaiyakun, Effect of deposition time on nanocolumnar TiZrN films grown by reactive magnetron co-sputtering with the OAD technique, Mater. Tehnol. 55 (2021) 65–70.
[15] R. Alvarez, S. Munoz-Pina, M.U. Gonzalez, I. Izquierdo-Barba, I. Fernandez-Martinez, V. Rico, D. Arcos, A. Garcia-Valenzuela, A. Palmero, M. Vallet-Regi, A. R. Gonzalez-Elipe, J.M. Garcia-Martin, Antibacterial nanostructured Ti coatings by magnetron sputtering: from laboratory scales to industrial reactors, Nanomaterials 9 (2019) 13.
[16] N. Ziegler, C. Sengstock, V. Mai, T.A. Schildhauer, M. Koller, A. Ludwig, Glancing-angle deposition of nanostructures on an implant material surface, Nanomaterials 9 (2019) 11.
[17] S. Bagherifard, D.J. Hickey, A.C. de Luca, V.N. Malheiro, A.E. Markaki, M. Guagliano, T.J. Webster, The influence of nanostructured features on bacterial adhesion and bone cell functions on severely shot peened 316L stainless steel, Biomaterials 73 (2015) 185–197.
[18] L.T. Liu, Y.Z. Li, K.P. Yu, M.Y. Zhu, H. Jiang, P. Yu, M.X. Huang, A novel stainless steel with intensive silver nanoparticles showing superior antibacterial property, Mater. Res. Lett. 9 (2021) 270–277.
[19] R. Alvarez, C. Lopez-Santos, J. Parra-Barranco, V. Rico, A. Barranco, J. Cotrino, A. R. Gonzalez-Elipe, A. Palmero, Nanocolumnar growth of thin films deposited at oblique angles: beyond the tangent rule, J. Vac. Sci. Technol. B 32 (2014) 041802.
[20] W.B. Qin, J.S. Li, Q.Z. Mao, Y.Y. Liu, Y.F. Liu, W. Jiang, J.J. Kang, Evolution of tribological mechanisms of nano-grained 304L stainless steel under dry and polyalphaolefin lubrication conditions, Mater. Lett. 242 (2019) 147–151.
[21] A. Garcia-Valenzuela, A. Fakhfouri, M. Oliva-Ramirez, V. Rico-Gavira, T.C. Rojas, R. Alvarez, S.B. Menzel, A. Palmero, A. Winkler, A.R. Gonzalez-Elipe, Patterning and control of the nanostructure in plasma thin films with acoustic waves: mechanical vs. electrical polarization effects, Mater. Horiz. 8 (2021) 515–524.
[22] I. Horcas, R. Fernandez, J.M. Gomez-Rodriguez, J. Colchero, J. Gomez-Herrero, A. M. Baro, WSXM: a software for scanning probe microscopy and a tool for nanotechnology, Rev. Sci. Instrum. 78 (2007) 8.
[23] M.Y. Jang, J.W. Park, S.Y. Baek, T.W. Kim, Anisotropic wetting characteristics of biomimetic rice leaf surface with asymmetric asperities, J. Nanosci. Nanotechnol. 20 (2020) 4331–4335.
[24] Q. Liu, J.P. Yu, H. Wang, The role of the substrate roughness in contact angle hysteresis and dynamic deviation, Int. J. Heat. Mass Transf. 148 (2020) 118985.
[25] C.G. Jothi Prakash, R. Prasanth, Approaches to design a surface with tunable wettability: a review on surface properties, J. Mater. Sci. 56 (2021) 108–135.
[26] C.G. Jange, R.P.K. Ambrose, Quantifying the influence of surface chemical composition on surface energy during powder flow, Part. Sci. Technol. 39 (2021) 192–203.
[27] R.N. Shimizu, N.R. Demarquette, Evaluation of surface energy of solid polymers using different models, J. Appl. Polym. Sci. 76 (2000) 1831–1845.
[28] J. Yang, J.Z. Bei, S.G. Wang, Enhanced cell affinity of poly (D,L-lactide) by combining plasma treatment with collagen anchorage, Biomaterials 23 (2002) 2607–2614.
[29] Y.K. Cai, W.L. Chang, X. Luo, A.M.L. Sousa, K.H.A. Lau, Y. Qin, Superhydrophobic structures on 316L stainless steel surfaces machined by nanosecond pulsed laser, Precis. Eng. J. Int. Soc. Precis. Eng. Nanotechnol. 52 (2018) 266–275.
[30] F.F. Eliyan, A. Alfantazi, Mechanisms of corrosion and electrochemical significance of metallurgy and environment with corrosion of iron and steel in bicarbonate and carbonate solutions-a review, Corrosion 70 (2014) 880–898.
[31] S.A. Schroder, S. Eickhardt, T. Bjarnsholt, T. Norgaard, P. Homoe, Morphological evidence of biofilm in chronic obstructive sialadenitis, J. Laryngol. Otol. 132 (2018) 611–614.
[32] R. Alvarez, A. Garcia-Valenzuela, V. Rico, J. Garcia-Martin, J. Cotrino, A. Gonzalez-Elipe, A. Palmero, Kinetic energy-induced growth regimes of nanocolumnar Ti thin films deposited by evaporation and magnetron sputtering, Nanotechnology 30 (2019) 475603.
[33] S. Mahato, J. Puigdollers, C. Voz, M. Mukhopadhyay, M. Mukherjee, S. Hazra, Near 5% DMSO is the best: a structural investigation of PEDOT: PSS thin films with strong emphasis on surface and interface for hybrid solar cell, Appl. Surf. Sci. 499 (2020) 143967.
[34] E. Paparazzo, , On the quantitative XPS analysis of Fe2O3 and Fe1-xO oxides, J. Electron Spectrosc. Relat. Phenom. 154 (2006) 38–40.
[35] G.D. Degaga, M. Trought, S. Nemsak, E.J. Crumlin, M. Seel, R. Pandey, K. A. Perrine, Investigation of N-2 adsorption on Fe3O4(001) using ambient pressure X-ray photoelectron spectroscopy and density functional theory, J. Chem. Phys. 152 (2020) 054717.
[36] A. Kadari, T. Schemme, D. Kadri, J. Wollschlaeger, XPS and morphological properties of Cr2O3 thin films grown by thermal evaporation method, Results Phys. 7 (2017) 3124–3129.
[37] M. Zandrahimi, M.R. Bateni, A. Poladi, J.A. Szpunar, The formation of martensite during wear of AISI 304 stainless steel, Wear 263 (2007) 674–678.
[38] D. Guo, C.T. Kwok, L.M. Tam, D. Zhang, X. Li, Hardness, microstructure and texture of friction surfaced 17-4PH precipitation hardening stainless steel coatings with and without subsequent aging, Surf. Coat. Technol. 402 (2020) 126302.
[39] A.M. Emelyanenko, F.M. Shagieva, A.G. Domantovsky, L.B. Boinovich, Nanosecond laser micro- and nanotexturing for the design of a superhydrophobic coating robust against long-term contact with water, cavitation, and abrasion, Appl. Surf. Sci. 332 (2015) 513–517.
[40] V. Rico, J. Mora, P. Garcia, A. Aguero, A. Borras, A.R. Gonzalez-Elipe, C. Lopez-Santos, Robust anti-icing superhydrophobic aluminum alloy surfaces by grafting fluorocarbon molecular chains, Appl. Mater. Today 21 (2020) 100815.
[41] N. Chi-Vinh, D.-M. Chun, Control of laser-ablated aluminum surface wettability to superhydrophobic or superhydrophilic through simple heat treatment or water boiling post-processing, Appl. Surf. Sci. 435 (2018) 974–982.
[42] D.-M. Chun, N. Chi-Vinh, K.-M. Lee, Fast fabrication of superhydrophobic metallic surface using nanosecond laser texturing and low-temperature annealing, Cirp Ann. Manuf. Technol. 65 (2016) 519–522.
[43] Z. Yang, X. Liu, Y. Tian, Insights into the wettability transition of nanosecond laser ablated surface under ambient air exposure (vol 533, pg 268, 2019), J. Colloid Interface Sci. 539 (2019), 672-672.

[44] J.W. Lu, Y. Zhang, W.T. Huo, W. Zhang, Y.Q. Zhao, Y.S. Zhang, Electrochemical corrosion characteristics and biocompatibility of nanostructured titanium for implants, Appl. Surf. Sci. 434 (2018) 63–72.
[45] U.K. Mudali, S. Ningshen, A.R. Shankar, Nanostructured coatings for corrosion protection in reprocessing plants, Pure Appl. Chem. 83 (2011) 2079–2087.
[46] J.L. Daure, K.T. Voisey, P.H. Shipway, D.A. Stewart, The effect of coating architecture and defects on the corrosion behaviour of a PVD multilayer Inconel 625/Cr coating, Surf. Coat. Technol. 324 (2017) 403–412.
[47] A. Zarebidaki, A. Seifoddini, T. Rabizadeh, Corrosion resistance of Fe77Mo5P9C7.5B1.5 in-situ metallic glass matrix composites, J. Alloy. Compd. 736 (2018) 17–21.
[48] A. Sanati, K. Raeissi, H. Edris, Investigation of the corrosion behavior of cathodic arc evaporated stainless steel coating in 3.5% NaCl, Prot. Met. Phys. Chem. Surf. 53 (2017) 902–909.
[49] C.R. Arciola, D. Campoccia, P. Speziale, L. Montanaro, J.W. Costerton, Biofilm formation in Staphylococcus implant infections. A review of molecular mechanisms and implications for biofilm-resistant materials, Biomaterials 33 (2012) 5967–5982.
[50] J. Wang, H. Zhou, G. Guo, J. Tan, Q. Wang, J. Tang, W. Liu, H. Shen, J. Li, X. Zhang, Enhanced anti-infective efficacy of ZnO nanoreservoirs through a combination of intrinsic anti-biofilm activity and reinforced innate defense, ACS Appl. Mater. Interfaces 9 (2017) 33609–33623.